Insights into the Nature of the Active Sites of Tin-Montmorillonite for the Synthesis of Polyoxymethylene Dimethyl Ethers (OME)

Christophe J. Baranowski,[a] Ali M. Bahmanpour,[a] Florent Héroguel,[a] Jeremy S. Luterbacher,[a] and Oliver Kröcher*[a, b]

In this study, we report that intercalation of tin into montmorillonite clay (Sn-MMT) boosts catalytic activity for the synthesis of polyoxymethylene dimethyl ethers, a promising diesel fuel additive. This increase in activity is attributed to the formation of a hierarchical catalyst displaying high surface area with accessible Brønsted and Lewis acid sites. Extensive characterization such as MAS-NMR, XRD and in-situ DRIFTS confirmed that tin insertion induced reorganization of the clay layers into a disorganized house-of-cards structure. It also revealed that tin resided between the clay layers as defective SnO_2 nanocrystals stabilized by the negative charge of MMT. The source of acidity in Sn-MMT was studied by comparing it with two similar materials, namely $Sn(OH)_4$, and thermally treated Sn-MMT. Low activity measured for isolated hydroxylated SnO_2 nanoparticles illustrates the importance of having clay and tin in close proximity. Meanwhile, deactivation upon thermal treatment occurred via sintering of the tin phase and diffusion of the protons inside the layers. Sn-MMT acidity is attributed to the combination of Si–OH–Al groups, formed as a by-product of SnO_2 crystallization, and undercoordinated Sn surface sites, stabilized by the negative charge of MMT.

Introduction

Despite their higher efficiency, diesel cars suffer from excessive NO_x emissions which has contributed to their bad reputation. Polyoxymethylene dimethyl ethers (OME) are a new class of biofuel that were recently introduced as potential diesel additive or substitute.[1–3] OME are oligomers composed of an oxymethylene chain capped by a methyl- and a methoxy-group, that drastically decreases the concentration of harmful pollutants in the exhaust gas (i.e. soot and NO_x) when blended with diesel fuel. Introduction of the OME technology could thus alleviate diesel-related air pollution. OME synthesis involves a methyl and an oxymethylene source and leads to a large range of chain lengths, which follows the Schulz-Flory product distribution. The anhydrous synthesis route, with trioxane (TRI) and dimethoxymethane (OME₁), is known to generate the highest yield of OME (Scheme 1).[4] Various catalysts such as zeolites, acidic resins or ionic liquids have been used for this synthesis route.[5–8] Solid acids have the intrinsic advantage of offering an easy separation compared to ionic liquids or mineral acids. It was found that both Brønsted[9,10] and Lewis[11,12] acidity catalyze OME synthesis. Currently, acidic resins and zeolite H-
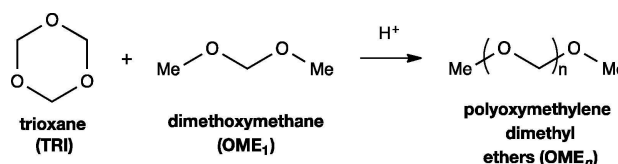
Scheme 1. Synthesis of polyoxymethylene dimethyl ether (OME) from dimethoxymethane (OME₁) and trioxane (TRI).

Beta have demonstrated the highest potential as catalyst for OME synthesis.[13,14] However, acidic resins can deactivate due to thermal instability.[15] Additionally, we demonstrated previously that H-ZSM-5 suffered from severe internal mass diffusion limitation, which could be circumvented by the addition of an auxiliary network of mesopores.[16] Development of catalysts displaying a high number of accessible acidic sites is thus required for efficient OME synthesis.

Meanwhile, clay has emerged over the past decades as a new type of cheap and eco-friendly material with versatile, high-end applications ranging from adsorbents to drilling fluids.[17,18] It is capable of catalyzing a wide range of reactions such as addition, oxidation or dehydration.[19,20] Its structure possesses advantageous features: it is composed of stacked aluminosilicate layers with intrinsic ion-exchange properties. Montmorillonite (MMT) is a 2:1 phyllosilicate clay with each layer composed of an octahedral alumina sheet sandwiched between two tetrahedral silica sheets.[21] Isomorphous substitution by lower valence atoms such as Ca(II), Al(III) or Mg(II) in the aluminosilicate lattice generates a net negative charge counterbalanced by cations between the layers. These properties were leveraged to generate new types of structures such as

[a] C. J. Baranowski, Dr. A. M. Bahmanpour, Dr. F. Héroguel, Prof. Dr. J. S. Luterbacher, Prof. Dr. O. Kröcher
Institute of Chemical Sciences and Engineering
École polytechnique fédérale de Lausanne (EPFL)
Route cantonale, 1015 Lausanne (Switzerland)
[b] Prof. Dr. O. Kröcher
Paul Scherrer Institut
5232 Villigen PSI (Switzerland)
E-mail: oliver.kroecher@psi.ch

delaminated clay or pillared layered clay (PILC), which are routinely used to catalyze various organic reactions. Notably, PILC can attain high accessible surface area with pore sizes larger than conventional zeolites.[22]

Introduction of tin by ion-exchange in MMT was recently shown to lead to a new catalytic material (Sn-MMT) following a simple procedure illustrated in Scheme 2.[23,24] Its advantageous

SnCl$_4$.5H$_2$O
4 hours, RT

Na-MMT

Sn-MMT
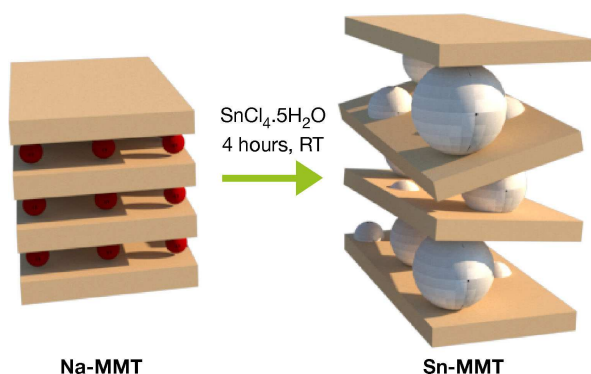
Scheme 2. Insertion of tin in between MMT layers.

textural and acidic properties, as well as its ease of preparation compared to other tin-containing heterogeneous catalysts, lead to its applications in various organic reactions. Wang et al. reported that Sn-MMT displayed a highly superior activity than Sn-grafted MCM-41 for the cyanosilylation of ketones.[25] They later found that its high specific surface area was formed by the intercalation of SnO$_2$ nanoparticles between clay layers, resulting in strong Brønsted and Lewis acidity.[26–28] Sn-MMT was also found to display a disorganized "house-of-cards" structure.[23] The coexistence of acid sites was leveraged for various hemicellulose upgrading reactions: conversion of carbohydrates to 5-(hydroxymethyl) furfural (HMF),[29] HMF self-etherification,[24] synthesis of alkyl lactates from triose[30] and the production of furfural from xylose.[31] Sn-MMT was also applied for the Baeyer-Villiger oxidation.[32]

A reaction mechanism involving chain-like polymers of SnO$_2$ in between the clay layers was suggested by Wang et al.[28] Masui et al. estimated that the contact domain between clay layers and hydroxylated SnO$_2$ nanoparticles was responsible for the material's catalytic activity.[23] Finally, an isolated Sn species was also referred to by Hara et al.[32] Despite this extensive research, the nature of Sn-MMT's acidity remains unclear. Therefore, this study aimed at elucidating its source of activity. Acid-treatment and insertion of tin were performed to introduce acidity in MMT. Activity of both catalysts for OME synthesis was subsequently assessed and compared with Amberlyst 36 (A36), a common acidic resin. From these results together with characterization data and control experiments, conclusions were drawn about the nature of the active sites in Sn-MMT.

Results and Discussion

First, the effects of tin insertion and acid-treatment (AT-MMT) on Na-MMT's structure and morphology are presented and discussed. Next, the activities of the synthesized catalysts for the production of OME are presented and compared to A36. The influence of reaction parameters is also analyzed for Sn-MMT, our best clay-based candidate. In order to clarify the nature of the active sites, we subsequently compare the activity of Sn-MMT to two similar materials, Sn-MMT-TT400 and tin hydroxide (Sn(OH)$_4$), which were similarly characterized. Finally, structure-activity relationships are discussed.

Structure and Morphology of Na-MMT, AT-MMT and Sn-MMT

MMT possesses ordered units at different dimensions.[33] The layer is the first unit with a thickness of around 1 nm and a lateral dimension between 1–2 μm. The second unit consists of tactoids, which are several layers stacked onto each other in a turbostratic structure. Aggregates constitute the third unit and are composed of several tactoids with various arrangements that depend on different factors, including the nature of the interlayer cation.

Micropores can be present between layers (e.g. slit-shaped pores, lenticular-shaped) and mesopores generally arise from the presence of intertactoid pores. Clusters of aggregates may form interaggregates pores which are large mesopores to macropores. N$_2$ physisorption was used to investigate the textural properties of the samples resulting from tin insertion and acid-treatment (Figure 1a, Table S1, Supporting Information). It is important to note that N$_2$ does not penetrate the interlayer space of unmodified MMT.[34] All clays possessed a type II isotherm with an H2 hysteresis loop closing vertically at p/p^0 of 0.44, which is typical for clay. Acid-treatment and insertion of tin increased the specific surface area from 69 to 119 and 269 m^{2}g^{-1}, respectively (Table S1). At low relative pressure, increased N$_2$ uptake for AT-MMT and Sn-MMT indicated an increase in the microporous surface area (S$_{micro}$). The mesoporous surface area (S$_{meso}$) increased from 38 to 70 and 149 m^{2}g^{-1} for AT-MMT and Sn-MMT, respectively. Acid-treatment of Na-MMT led to layer delamination (Figure 1d) and to almost 90% replacement of interlayer Na$^+$ by H$^+$ (Table S2). Other cations present in the interlamellar space were also partly removed (e.g. K$^+$, Ca^{2+}). Mild clay dealumination was also observed, with its Si/Al molar ratio going up from 2.98 to 3.13. Furthermore, other substituting atoms (i.e. Mg^{2+} and Fe^{2+}) were also partly removed by the acid treatment, as the Si/Mg and Si/Fe molar ratios increased from 17.13 to 20.61 and from 24.05 to 25.94, respectively.

Meanwhile, despite Sn-MMT having a larger S$_{meso}$ compared to AT-MMT, it possessed a similar mesoporous volume, which could indicate the presence of interlayer tin. Sn-MMT possessed a broader distribution of small mesopores as well as fewer large mesopores (Figure 1a, inset). ICP-OES analysis (Table S2) revealed that upon ion-exchange with SnCl$_4$, Sn-MMT reached 27.8 wt.% of tin with only 660 ppm of sodium. SEM-EDX
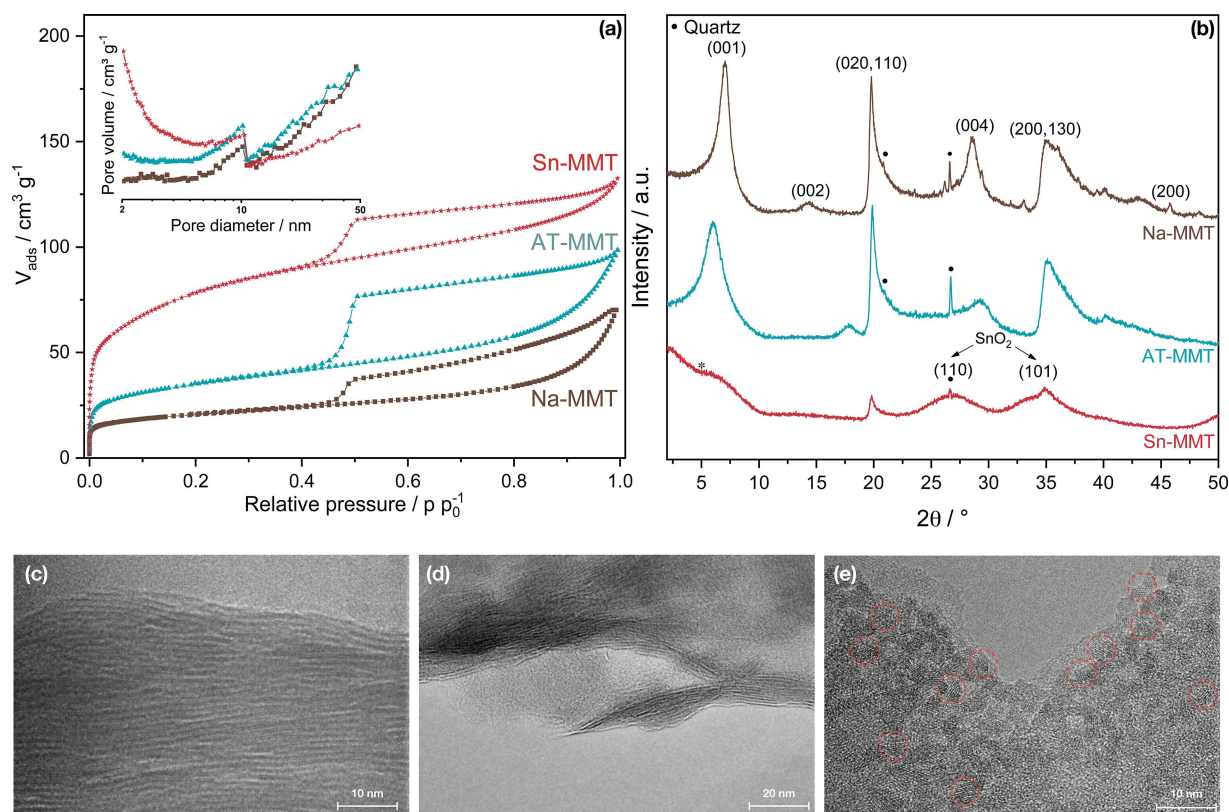
Figure 1. (a) N_2 isotherms of the catalyst samples and incremental pore volume determined using the BJH method (inset), (b) powder X-ray diffraction patterns of the catalyst samples (* indicates peak related to the sample holder) and TEM images of (c) Na-MMT, (d) AT-MMT, (e) Sn-MMT. Dotted circles are highlighting examples of lattice fringes observed for Sn-MMT.

confirmed that tin was homogeneously distributed in the clay particles as no tin aggregation was detected (Figure S2). The Si/ Al molar ratio remained constant after tin insertion which indicates that no composition modifications occurred to the aluminosilicate sheets.

X-ray diffraction patterns (Figure 1b) were used to investigate the clay structure and the nature of the tin phase. Na-MMT was identified with the (00 *l*) reflection at 7.0°, 14.2° and 28.6° as well as with the (020,110) and (200,130) reflections with maxima located at 19.9° and 34.9°, respectively.[35,36] The (001), (002) and (004) reflections of Sn-MMT almost disappeared showing a complete loss of the layered structure (confirming delamination) as well as a shift to lower diffraction angle, implying an increase in the mean interlayer distance from 1.24 nm to 1.31 nm (calculated using Bragg's law).[23,37] A broad (001) basal reflection is observed for AT-MMT which hence only suffered from partial layer stacking loss and an increase in the mean interlayer distance to 1.45 nm. Retention of the (020,110) and (200,130) reflections intensity suggested preservation of the two-dimensional structure (i.e. the clay sheets) for both Sn-MMT and AT-MMT.[38]

Sn-MMT displayed diffraction peaks characteristic of a rutile-type SnO_2 structure with broad peaks at 26.7° and 34.8°, corresponding to the (110) and (101) reflections, respectively.[23] The presence of broad peaks points to the formation of small, well-dispersed nanocrystals (below 5 nm). Combined with the porosity results, we deduced that these crystals were inserted

between the clay layers. Our results are thus in agreement with the report from Masui et al., stating that the presence of a nanocrystalline SnO_2 phase changed the staking arrangement of tactoids into a disordered 'house-of-card' structure.[23] Sn-MMT displayed the largest S_{micro}, as the presence of SnO_2 nanocrystals likely induced the formation of additional inter-layer microporous volume. The presence of interlayer SnO_2 was confirmed by bright field transmission electron microscopy, where lattice fringe contrasts were observed (Figure 1e). Due to the sensitive nature of the interlayer SnO_2 particles, no elemental analysis study was performed, as prolonged exposure to the electron beam lead to aggregation of the SnO_2 crystals. The presence of (110) and (101) SnO_2 planes was confirmed by selected area electron diffraction (Figure S3).

Diffuse reflectance infrared Fourier transform spectroscopy (DRIFTS) was carried out to gather additional information on the modifications of the clays (Figure S4). Due to the diversity of structural groups present, interpretation of the curves can sometimes be intricate due to peak overlapping. Samples containing MMT displayed two peaks corresponding to structural hydroxyl groups bounded to octahedral Al in the OH stretching and bending regions, respectively at 3623 and 917 cm^{-1}.[39] Acid-treatment resulted in decrease of the peaks at 917, 875 and 836 cm^{-1}, assigned to bending vibrations of the hydroxyl groups (Al$_2$OH), (AlFeOH) and (AlMgOH), respectively.[38] Mg^{2+} was more prone to leaching upon acid-
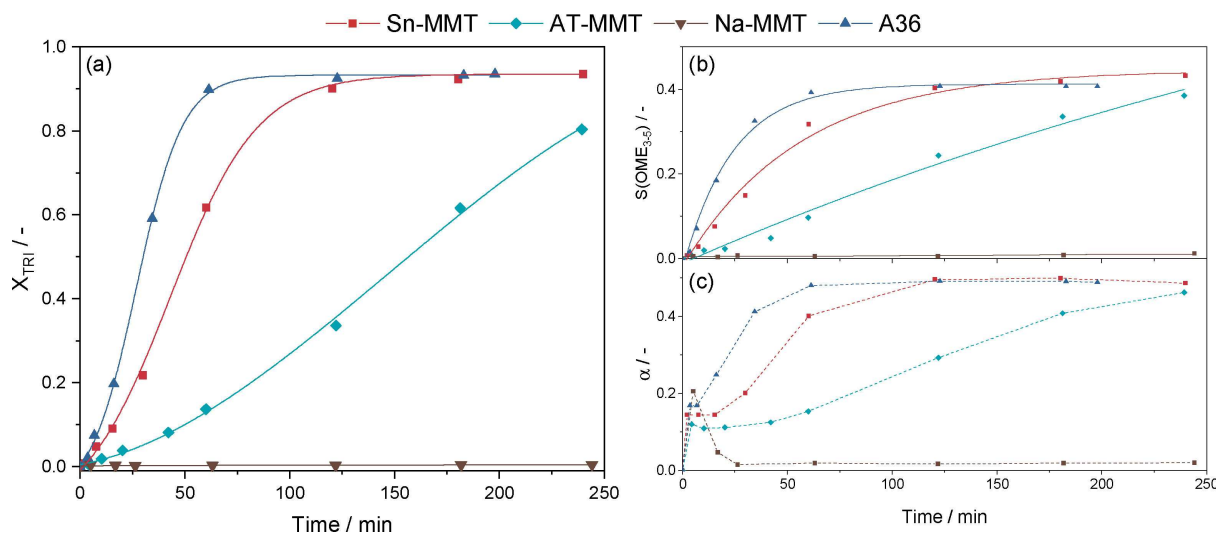
Figure 2. (a) TRI conversion X_{TRI}, (b) selectivity to OME_{3-5} $S(OME_{3-5})$ and (c) chain growth probability α for the production of OME.

treatment than Fe^{3+}.[40] The presence of chemisorbed and physisorbed water, most probably due to the hydration layer of the cations, was detected at 1630 cm^{-1} and 3423 cm^{-1}. Additionally, The Si—O out-of-plane and in-plane stretching peaks were identified at 1110 and 995 cm^{-1}, respectively. We observed a shift in both signals with the various treatments, which could be due to the change in the interlayer water content. These vibrations were independent of the nature or the concentration of the interlayer cation.[41] A detailed analysis of Sn-MMT spectrum is provided later.

Magic angle spinning nuclear magnetic resonance (MAS-NMR) was used to investigate the local structure of Si and Al atoms. Natural MMT contains paramagnetic and/or ferromagnetic species that make MAS-NMR analysis difficult.[42] Substitution of Si^{4+} by Al^{3+} in the tetrahedral sheet and substitution of Al^{3+} by Mg^{2+} in the octahedral sheet also induced broader peaks. ^{27}Al MAS-NMR (Figure S5) shows two resonance peaks at ca. 70 and 5 ppm, which are attributed to four-fold $Al^{(IV)}$ (tetrahedral sheet) and six-fold $Al^{(VI)}$ (octahedral sheet), respectively.[42–44] Overall, the proportion of $Al^{(VI)}$ to $Al^{(IV)}$ did not change significantly, indicating that the sheet structure stayed intact during acid-treatment or $SnCl_4$ ion-exchange.

The ^{29}Si MAS-NMR spectrum of Na-MMT shows a broad peak corresponding to $Q_3(0Al)$ (silicon atom connected to 3 silicon atoms via a basal oxygen and to the octahedral layer via an apical tricoordinated oxygen) (Figure S6). The chemical shift of $Q_3(0Al)$ depends on the nature of the interlayer cation[45] and shifts towards higher frequencies with a lower amount of Na^+ cations in the interlamellar space. Specifically, this peak appears at -90.5, -93.0 or -93.8 ppm for Na-MMT, AT-MMT and Sn-MMT, respectively. A shoulder centered at ca. -83, -89 or -90 ppm for Na-MMT, AT-MMT and Sn-MMT, respectively, corresponds to a $Q_3(1Al)$ moiety (silicon atom connected to 2 silicon and 1 aluminum atoms via bridging oxygens and to the octahedral sheet via an apical oxygen).[45] Finally, the acid-

treatment results in the appearance of a peak for Q_3 ($SiO\equiv Si-OH$) due to dealumination.

Catalytic Properties for OME Synthesis

TRI conversion, selectivity towards OME_{3-5} as well as chain growth probability vs. time are displayed in Figure 2 for various MMT samples and for A36. Their activities followed the trend: A36 > Sn-MMT > AT-MMT > Na-MMT. Na-MMT showed almost no TRI conversion but both treatments applied on the clay significantly improved its activity. AT-MMT possessed a modest activity while Sn-MMT performance was close to A36, our reference material. The latter reached equilibrium after 120 min of reaction while 180 min were necessary for Sn-MMT to achieve the same results. AT-MMT did not reach equilibrium during the experimental run time. Sn-MMT led to a higher selectivity of 0.44 to OME_{3-5} at the end of the run compared to 0.41 using A36 (Figure 2b). Both catalysts led to an equal value of α, which reflects a chain length distribution that followed the SF distribution (Figure 2c).

A more detailed study on the influence of reaction parameters was performed using Sn-MMT as the most active MMT-based candidate for the synthesis of OME (Figure 3). Increase of the reaction temperature resulted in a lower TRI conversion and α value at equilibrium as expected for an exothermic reaction (Figure 3a). Additionally, TRI conversion and α increased linearly with catalyst concentration (Figure 3b). As expected, changing the molar ratio of OME_1/TRI affected both TRI conversion and α at equilibrium (Figure 3c): decreasing the ratio diminished the TRI conversion but increased α, while an increase in the ratio resulted in higher TRI conversion with smaller α. Indeed, increasing the proportion of TRI increases the OME chain length distribution at the expense of TRI conversion at equilibrium; this parameter thus needs to be optimized to maximize the production of OME_{3-5}. Stability of Sn-MMT and
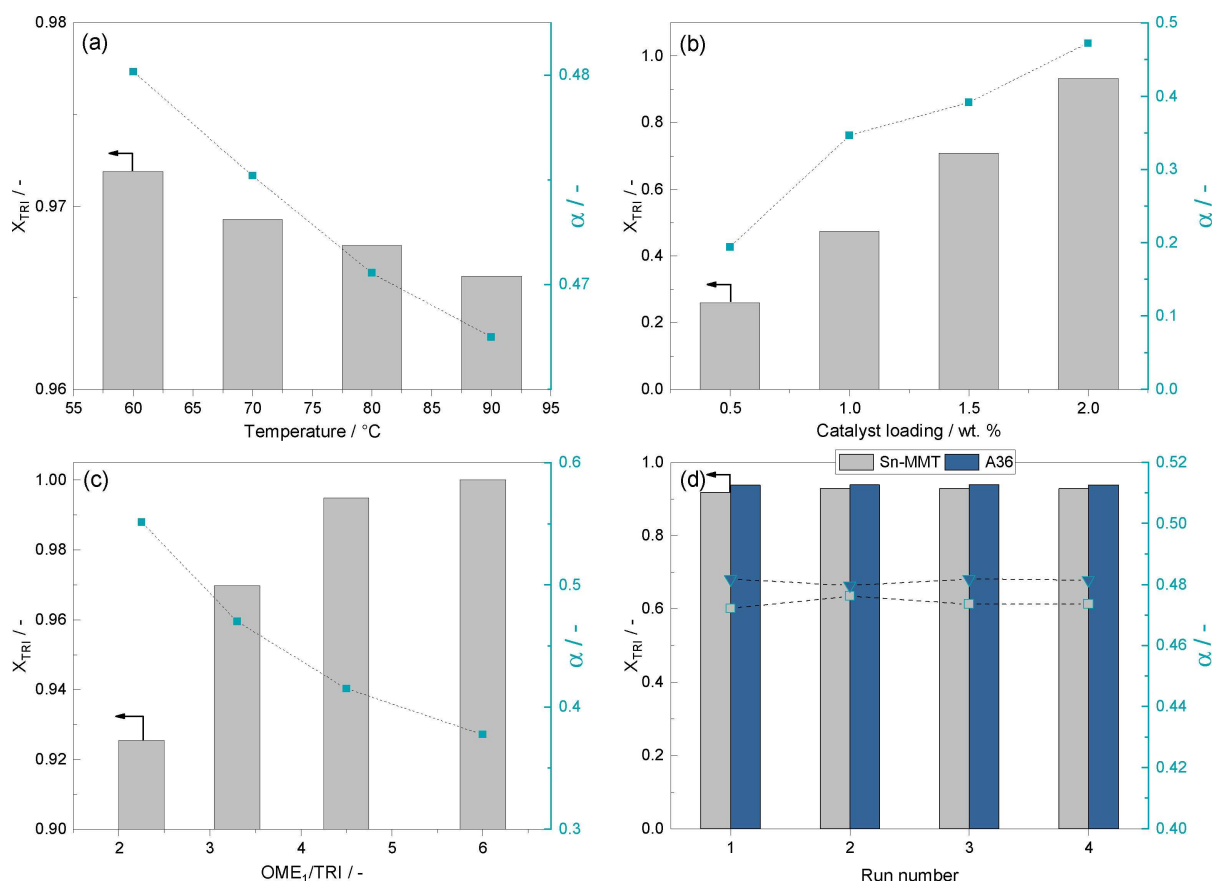
Figure 3. OME synthesis from OME$_1$ and TRI. TRI conversion X_{TRI} and chain growth probability α (a) at equilibrium for various temperature (0.5 wt.% Sn-MMT, reaction time 240 min), (b) at various Sn-MMT wt.% (reaction time 30 min), (c) at equilibrium for different OME$_1$/ TRI molar ratio (0.5 wt.% Sn-MMT, reaction time 240 min) and (d) in a reusability test with A36 and Sn-MMT (1.0 wt.%, reaction time 60 min).

A36 was also assessed during 4 successive runs (Figure 3d) where comparable activities and no deactivation was observed.

Catalytic Properties and Characterization of SnO$_2$ Catalysts

In order to shed more light on the source of acidity of Sn-MMT, we studied the activity of two similar materials: Sn-MMT-TT400 (obtained after calcination at 400 °C for 3 hours of Sn-MMT) and tin hydroxide (Sn(OH)$_4$, synthesized by reduction of SnCl$_4$). They help to understand the effect of calcination on the performance of Sn-MMT, and the interaction between clay and tin. Previous studies already used a similar comparison for a different reaction but failed to provide a detailed explanation on their lack of activity in comparison with Sn-MMT.[23,24] As expected, both catalysts displayed much lower activity compared to Sn-MMT for the synthesis of OME from TRI and OME$_1$ (Figure 4). Thermal treatment showed a drastic effect on the TRI conversion with a drop of 92% while a TRI conversion of only 2.3% was reached using Sn(OH)$_4$.

A careful characterization of Sn-MMT-TT400 and Sn(OH)$_4$ has been performed in order to build structure-activity relationships. Sn-MMT, Sn-MMT-TT400 and Sn(OH)$_4$ displayed diffraction peaks characteristic of SnO$_2$ structure (Figure S7b) with average

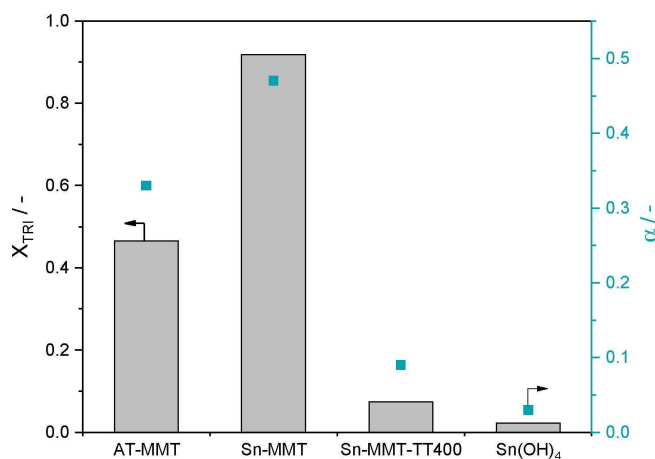**Figure 4.** TRI conversion X_{TRI} and chain growth probability α for AT-MMT, Sn-MMT, Sn-MMT-TT400 and Sn(OH)$_4$ (1.0 wt.% catalyst, reaction time 60 min).

crystallite sizes of 2.74, 4.82 and 3.04 nm, respectively (calculated based on the (001) reflection using Scherrer's equation). The thermal treatment of Sn-MMT slightly affected the (020,110) and (200,130) reflections, which could indicate a change in the clay layer crystal lattice. Additionally, N$_2$
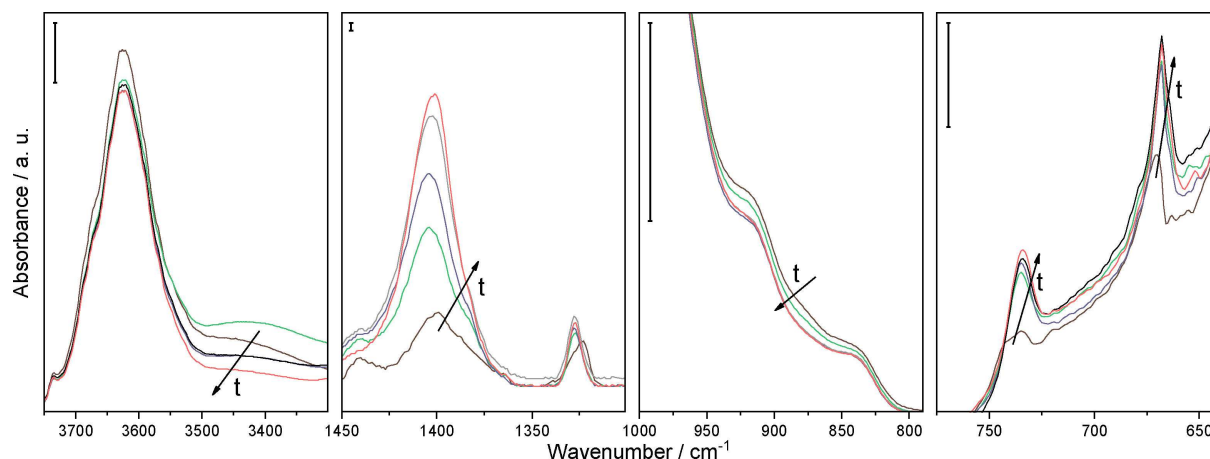
Figure 5. In-situ DRIFT spectra of Sn-MMT treated at 400 °C under 20 mL min^{-1} of He at various times (the scale bar on the top left of each frame indicates the relative intensity).

physisorption suggests sintering of SnO$_2$ nanocrystals upon thermal treatment with a decrease in S$_{micro}$ while S$_{meso}$ remained rather constant (Table S1, Figure S7a). Sn(OH)$_4$ displayed a type I isotherm (S$_{micro}$ of 75 m^{2}g^{-1} and S$_{meso}$ of 46 m^{2}g^{-1}) and confirms the high porosity of the tin hydroxide phase.

In order to get more insight into the deactivation mechanism of Sn-MMT during the thermal treatment, we performed in-situ DRIFTS of Sn-MMT at 400 °C (Figure 5). An increase in vibrations related to symmetric O–Sn–O and antisymmetric Sn–O–Sn stretching mode of a surface bridging oxide was observed at 669 and 737 cm^{-1}, respectively, which is attributed to sintering of SnO$_2$ nanocrystals.[46] The peaks at 1327 and 1415 cm^{-1} are overtones of these two vibrations. Furthermore, we also observed a decrease of the signal between 850 and 950 cm^{-1} that corresponds to the hydroxyl bending region.

This phenomenon was ascribed by Alvero et al. to the migration of cations in vacant hexagonal holes of the silica sheet where they interact with structural hydroxyl groups.[47] Meanwhile, analysis of the hydroxyl stretching region showed a decrease of a broad peak between 3300 and 3500 cm^{-1}, which can be attributed to dehydration of the clay and/or condensation of Sn-OH groups. No change was identified in the Si–OH (ca. 3740 cm^{-1}) and Al-OH regions (3640 cm^{-1}).

Comparison between ex-situ DRIFT spectra of Sn-MMT and Sn-MMT-TT400 shows a large difference in the intensity of the OH stretching region between 3500 and 3300 cm^{-1} due to irreversible desorption of both chemisorbed water and hydroxyl surface groups (Figure S8). When the hydration shell of the proton is removed at high temperature, H$^+$ migrates in the clay sheet, thereby neutralizing its net charge, a phenomenon known as the Hofmann-Klemen effect. This was confirmed by a slight shift in the Si–O–Si stretching vibration which could result from lattice distortion of the Si–O framework due to the presence of the proton.[47] This corroborates with the XRD patterns showing a weakening of the (020,110) reflection. Furthermore, a similar decrease of the signal intensity between 850 to 950 cm^{-1} was observed compared to the in-situ DRIFTS measurements. The effect of the thermal treatment of the clay

was also observed with ^{27}Si MAS-NMR spectroscopy showing a shift of the Q3(0Al) peak from −93.8 to −95.1 ppm, which is attributed to the formation of a neutral structure (Figure S6).[48] Overall, it appeared that during the thermal treatment, the interlayer water was removed, dehydroxylated SnO$_2$ nanocrystals sintered, and protons migrated inside the clay layers.

Meanwhile, analysis of Sn(OH)$_4$ DRIFT spectrum shows a broad peak around 3440 cm^{-1} corresponding to the O–H stretching vibration from the hydroxylated surface and molecular water, also responsible for the peak at 1630 cm^{-1} (Figure S8). Saturation of the signal occurred at wavenumbers below 680 cm^{-1} due to the strong signal from Sn–O–Sn stretching vibration.[46]

The local structure of Sn was also investigated by ^{119}Sn MAS-NMR (Figure 6a). All samples have similar signals with a main peak centered around −604 ppm, which can be ascribed to octahedral tin in bulk SnO$_2$.[49] No tetrahedral tin was detected. Variation of the main peak can be the result of hydroxylation of SnO$_2$ surface and its crystalline size.[50] Peak broadening indicates the presence of SnO$_2$ nanocrystals as surface atoms have different chemical shifts compared to bulk atoms. Hydroxylation of the tin surface was indicated by signals of the first and second tin layer which have chemical shifts of −590 and −615 ppm, respectively (Figure 6a, inset).[23,51] Sn-MMT-TT400 and Sn-MMT appear to have a slight signal shift towards lower values compared to Sn(OH)$_4$. We suggest that this is caused by covalent anchoring of Sn atoms to the clay sheet to one or two silicon atoms via an oxygen bridge.[52] Thermal treatment would thus also increase the number of covalent bonds between SnO$_2$ and the tetrahedral silica sheet. A similar anchoring mechanism was observed for Al-pillared MMT upon thermal treatment.

For further analysis of the oxidation states of the surface SnO$_2$ species, we employed XPS which provides small probing depth in contrast to MAS-NMR (Figure 6b). The high-resolution Sn 3d$_{5/2}$ XPS spectra of Sn(OH)$_4$ were deconvoluted into two peaks attributed to Sn^{2+} and Sn^{4+}, respectively centered at 486.8 and 487.3 eV.[53] Figure 7b demonstrates that the tin
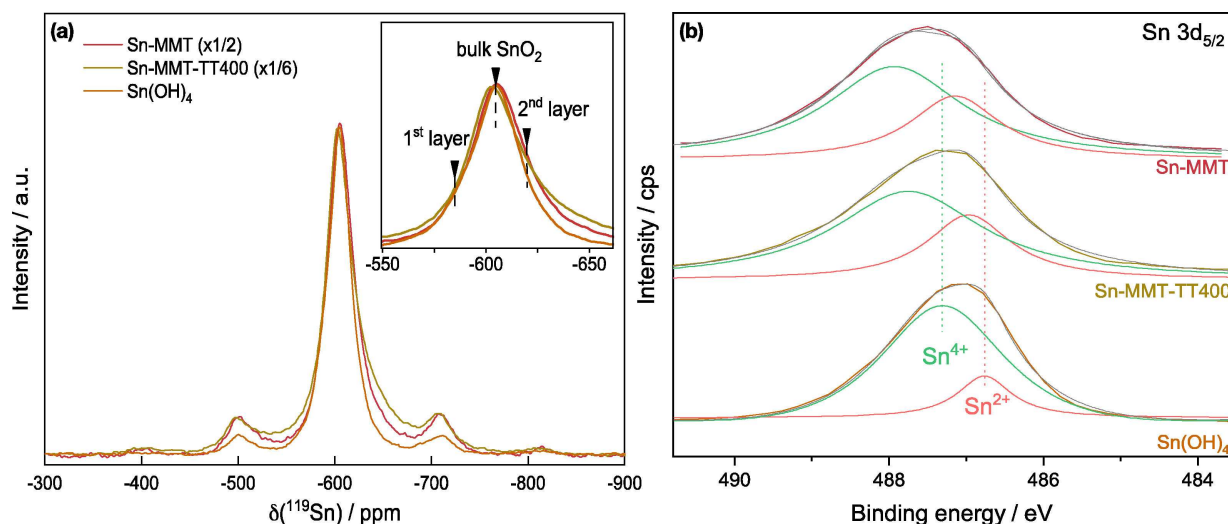
Figure 6. (a) ^{119}Sn MAS-NMR spectra and enlarged view of the main peak (inset). (b) Deconvolution of the main XPS peak of Sn-MMT, Sn-MMT-TT400 and Sn(OH)$_4$.
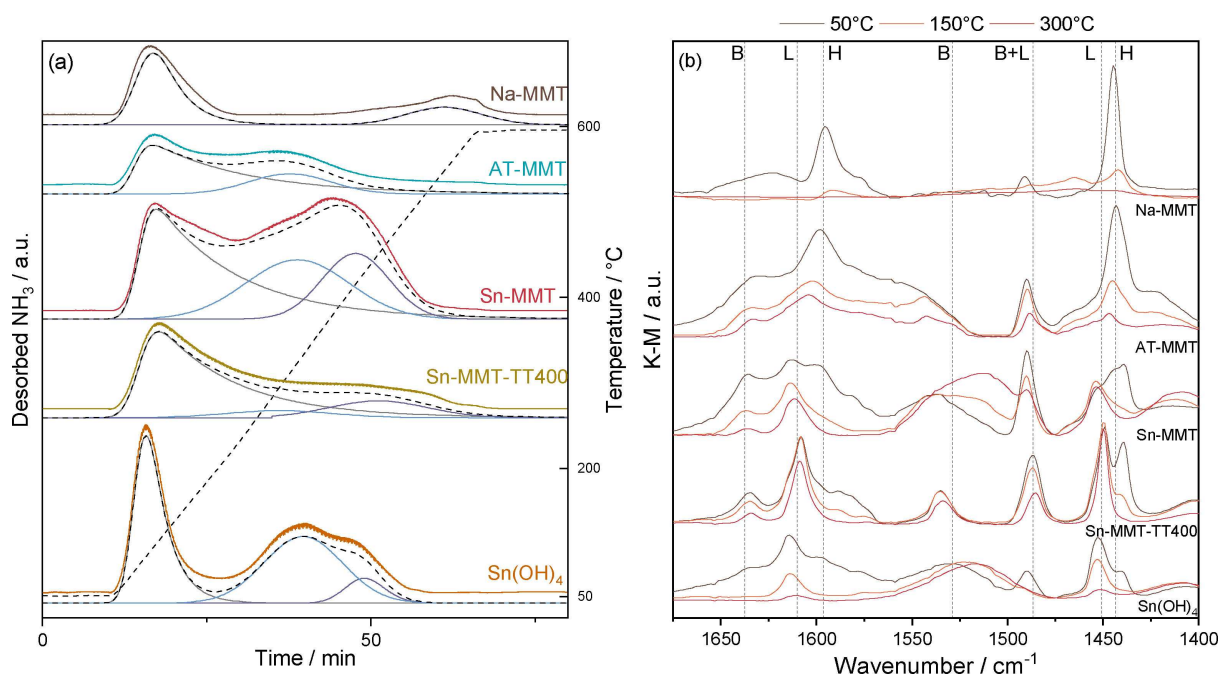

Figure 7. Characterization of the acidity of the catalysts by (a) NH$_3$-TPD and (b) pyridine-FTIR spectroscopy at various temperatures (B and L indicate pyridine bonded to Brønsted and Lewis sites, respectively, while H indicates H-bonded pyridine).

prevalently existed as Sn^{2+} compared to Sn^{2+}, which is an aliovalent substitution that require a charge compensation mechanism (i.e. an oxygen vacancy). In comparison, tin species residing between the clay exhibited two differences: a higher proportion of Sn^{2+} and a shift of both peaks towards higher binding energies (Table S3). According to Yang et al., a shift towards higher binding energies reflects a surface with a higher amount of oxygen vacancies.[54] Being positively charged, they cause a decrease in the electron density of nearby Sn, and thus an increase in their binding energies. Thus, we suggest that the

negative charge of the aluminosilicate layers induced a higher number of structural defects during crystallization of SnO$_2$ in the interlamellar space (i.e. Sn^{2+} and adjacent oxygen vacancies). Therefore, the activity of Sn-MMT could be due to a higher number of oxygen vacancies and adjacent undercoordinated Sn^{2+} atoms on the surface, which were also demonstrated to be more active in NO$_2$ sensing.[55] Thermal treatment of Sn-MMT resulted in a shift towards lower binding energy but did not affect the proportion of Sn^{2+}/Sn^{4+}. Compared to Sn-MMT, Sn-MMT-TT400 displayed thus a lower amount of undercoordi-
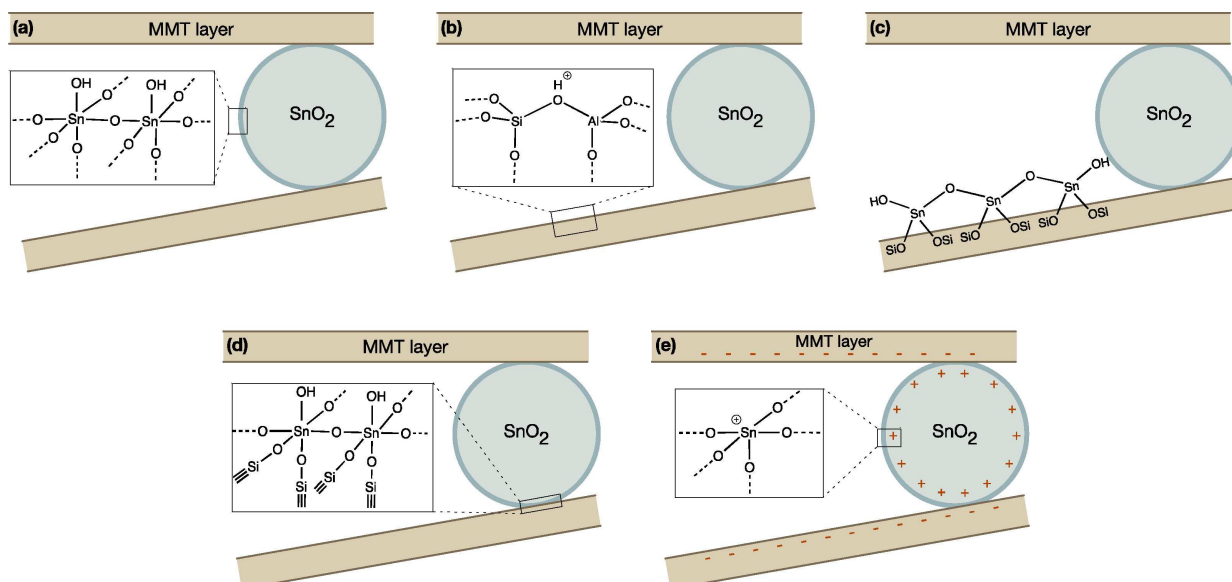
Scheme 3. Schematic representation of the possible acid sites of Sn-MMT.

nated surface Sn. Analysis of the O1s peak would not provide more information since it would also contain a large contribution from oxygen moieties present in the clay layer.

Acidic Properties of the Catalysts

Sample acidity was studied by NH_3-TPD (Figure 7a) and py-FTIR (Figure 7b). The NH_3-TPD profiles may not be perfectly reliable at temperature above 400 °C as structural changes may occur above this temperature. Acidity was measured by deconvolution of the NH_3-TPD profiles and these values are presented in Table S1. While Na-MMT had very low acidity (0.17 mmol·g^{-1}), exchanging interlamellar Na$^+$ cations with H$^+$ (AT-MMT) increased its acidity to 0.31 mmol·g^{-1}. Thermal treatment of Sn-MMT decreased acid site concentration from 0.71 to 0.51 mmol·g^{-1} but did not alter the nature and strength of the acid sites with no difference observed by FTIR spectroscopy after saturation with pyridine vapor at 50 °C.[56] The typical bands for Brønsted (1530 and 1365 cm^{-1}), Lewis (1451 and 1609 cm^{-1}) and H-bonded pyridine (1444 and 1596 cm^{-1}) acidity were observed for Sn-MMT and Sn-MMT-TT400. The signal corresponding to Lewis acid sites remained constant with increasing temperatures, while the signal corresponding to Brønsted acid sites slightly diminished. Thus, both catalysts displayed strong Lewis acid sites and moderate Brønsted acidity. Meanwhile, weak and moderate Brønsted acidity were identified for Na-MMT and AT-MMT, respectively. Finally, Sn(OH)$_4$ mostly displayed Lewis acid sites of moderate strength (0.61 mmol·g^{-1}).

Discussion on the Nature of the Active Site

The characterization data obtained in this study helped to shed more light on Sn-MMT structure and active sites. Upon ion-exchange with tin chloride, SnO$_2$ nanocrystals were formed in between MMT layers by Sn^{4+} hydrolysis according to Equation (1). As a result, clay layers were opened and exposed. Sn-MMT displayed a high surface area, as well as higher accessibility to strong acid sites due to the presence of micro- and mesopores.

$$SnCl_4 + 4\,H_2O + 4\,Na^+ \rightarrow Sn(OH)_4 + 4\,NaCl + 4\,H^+ \qquad (1)$$

Comparison of the catalytic activity of Sn-MMT, Sn-MMT-TT400 and Sn(OH)$_4$ in OME synthesis, combined with the catalysts' characterization data allowed us to clarify the nature of the acid sites present in Sn-MMT (Scheme 3). The first question to answer is whether the acidity comes from the clay layer, the SnO$_2$ nanocrystals, or both. First, since the activity of Sn(OH)$_4$ was the lowest among these three catalysts, it is clear that the SnO$_2$ nanocrystals have to be within the clay layers to efficiently catalyze OME synthesis. Surface Sn atoms acting as moderate Lewis acid and hydroxyl groups on the surface of the nanocrystals are insufficient to catalyze OME synthesis (Scheme 3a). Therefore, the proposal of Shinde et al. that hydroxylated SnO$_2$ nanocrystals act as a source of Brønsted acidity is invalid.[24]

Second, the clay layer is known to expose only weak Brønsted-acidic silanols and weak Lewis acid sites (i.e. under-coordinated Al^{3+} or Mg^{2+} at the edge of the clay sheet). Acidic protons could be produced during Equation (1) and stabilized by the clay layer (Scheme 3b). These protons could migrate into the clay layer during the thermal treatment, neutralizing the

clay positive charge and reducing its acidity. However, these acidic protons are known to be of moderate strength.[57]

Similar to pillaring of MMT with aluminum, we thus suggest that acidity is most probably linked to the combination of SnO_2 and the clay layers. Depending on the coordination and environment of Sn, several scenarios are possible. First, isolated, fourfold-coordinated Sn bound to 3 O—Si and one hydroxyl group could be the source of its acidity where SnO_2 nanocrystals would only serve as pillars to increase the surface area of MMT (Scheme 3c). Thermal treatment would cause them to migrate and coalesce with the SnO_2 nanocrystals and hence to lose their activity. However, fourfold-coordinated tin atoms were not detected by ^{119}Sn MAS-NMR.

Secondly, interfacial Sn atoms, anchored to the clay layer, could act as the source of Brønsted acidity (Scheme 3d). However, it would be rather unlikely that surface Sn could act both as cross-linking point to the clay layers as well as acid sites. Only four-fold coordinated Sn, present on high energy facets such as the (111) and the (221) facets, could simultaneously coordinate to the clay layer and a hydroxyl group. Furthermore, access to these sites to OME molecules would be rather difficult.

Considering ^{119}Sn MAS-NMR and XPS data, showing that clay stabilized the formation of defective SnO_2 nanocrystals displaying a higher number of undercoordinated surface Sn^{2+} atoms, we believe that these defects act as strong Lewis acid sites (Scheme 3e). Undercoordinated surfaces sites of nanocrystals are electron deficient and are known to display a Lewis-acidic character.[58] Thermal treatment of Sn-MMT would cause sintering of the SnO_2 nanocrystals and migration of H^+ inside the clay. The resulting catalyst would contain neutral SnO_2 nanocrystal devoid of its acidity.

Acidity characterization showed that strong Lewis and moderate Brønsted acid sites were present. Furthermore, it demonstrated that thermal treatment affected mostly the acid site concentration. Therefore, we suggest that the source of Sn-MMT acidity is a combination of: (1) Si—OH—Al groups, produced during the crystallization of SnO_2 by the release of HCl (Scheme 3b) and (2) strong Lewis acid sites at the SnO_2 surface formed by undercoordinated Sn^{2+} surface atoms stabilized by the negative charge of the clay layer (Scheme 3e). The presence of both Lewis and Brønsted acid sites explains the observed high activity of Sn-MMT for OME synthesis. Liu et al. recently suggested a synergistic effect of Brønsted and Lewis acid sites for the synthesis of OME from paraformaldehyde and OME_1.[59] The Lewis acidity in $Sn(OH)_4$ alone was insufficient to catalyze OME synthesis, while the Brønsted acidity in AT-MMT resulted in only moderate activity. Besides acidity, the presence of both micro- and mesopores in Sn-MMT also allowed enhanced mass transport for bulky OME molecules.

Conclusions

We reported that tin incorporation into clay-based materials boost the catalytic activity for OME synthesis to reach similar performances compared to reference acidic resins. Based on detailed characterization, we gained insights into Sn-MMT active sites nature: upon ion-exchange with $SnCl_4$, SnO_2 nanocrystals were formed and expanded the MMT layers to produce accessible Brønsted and Lewis acid sites, leading to a disorganized house-of-cards structure. Control experiments revealed that hydroxylated tin oxide alone is a poor catalyst for OME synthesis. Moreover, Sn-MMT deactivates by losing its acidity upon thermal treatment, which occurs via successive dehydration, sintering of the SnO_2 phase and migration of protons within the clay layers. Sn-MMT acidity is attributed to Si—OH—Al group, formed as a by-product of SnO_2 crystallization, and undercoordinated, defective SnO_2 surface sites. The negative charge generated by the MMT layers is key in stabilizing these surface defects, which act as strong Lewis acid sites. In conclusion, our work thus identifies the active sites present in Sn-MMT and provides a first instance of clay-based catalysts for the synthesis of OME.

Experimental Section

Chemicals and Materials Synthesis

All reagents were of analytical grade and obtained from commercial suppliers. No further purification was done unless specified otherwise. Sodium-exchanged montmorillonite (Na-MMT) was purchased from Fluorochem. Trioxane (99%), dimethoxymethane (99.0%), $SnCl_4 \cdot 5H_2O$ and Amberlyst 36 (A36) were obtained from Sigma Aldrich. OME_2 to OME_6 (99.0%) were purchased from ASG Analytics.

Acid- and Tin Chloride Treatment

The acid-treated montmorillonite (AT-MMT) was prepared as described in a protocol given by Beloufa et al.[60] Crushed clay (30 g) was dispersed in 120 mL of Deionized water and the mixture was stirred for 2 h at room temperature in an Erlenmeyer flask. Then, 100 mL of a 0.5 M sulfuric acid aqueous solution was added. The solution was maintained for 2 days under stirring at room temperature. The mixture was then filtered and washed with distilled water until pH 7 was reached. Finally, the product was dried for 24 h at 110°C and crushed in a mortar.

Sn-MMT was prepared as described in a protocol given by Shinde et al.[24] Na-MMT (5.0 g) was stirred at room temperature in 80 mL of a 0.3 M aqueous $SnCl_4$ solution for 4 h. The clay was then collected by filtration and washed with distilled water until a pH 7 was reached. The product was then dried for 24 h at 110°C and crushed in a mortar. Sn-MMT-TT400 was obtained by thermal treatment of Sn-MMT at 400°C for 3 h under static air with a temperature ramp of 5°C min^{-1}. Hydroxylated SnO_2 nanoparticles (denoted as $Sn(OH)_4$) were prepared by hydrolysis of Sn^{4+} in a basic aqueous solution, by mixing a $SnCl_4$ aqueous solution (0.3 M, 100 mL) with 30% aqueous ammonia (26 mL) at room temperature.[61] The white precipitate was filtered and dried at 110°C overnight.

Material Characterization

N_2 physisorption experiments were performed on a Micrometrics 3Flex apparatus at liquid nitrogen temperature and N_2 relative pressures between 10^{-5} and 0.99. Typically, samples (ca. 150 mg) were dried at 120°C (temperature ramp 5°C min^{-1}) for 5 h under

vacuum. A leak test was performed before the analysis. Brunauer-Emmett-Teller (BET) surface, Barrett-Joyner-Helenda (BJH) and t-plot method were used to calculate the specific surface area, the mesoporous and microporous volume, respectively.

Elemental analyses were performed using inductively coupled plasma optical emission spectrometry (ICP-OES) at the Paul Scherrer Institute on a Vista pro AX Varian instrument. Clays were dissolved using a 1:2:2:2 mixture of HCl (30 wt.%), HNO_3 (65 wt.%), H_2SO_4 (96 wt.%) and HF (40 wt.%). XPS spectra were measured on a PHI VersaProbe II scanning XPS microprobe (Physical Instruments AG, Germany) with a monochromatic Al Kα X-ray source of 24.8 W power and a 100 μm beam size.

X-ray diffraction (XRD) patterns were recorded using a D8 advance Bruker instrument equipped with a 1D-LynxEye detector (Cu Kα radiation, no monochromator, Ni filter) with a step size of 0.01°. Structure of the sample was observed by transmission electron microscopy (TEM) on a FEI Tecnai Osiris with 200 kV acceleration voltage. Grids were prepared by deposition of a drop of ethanol suspension (99.8%, Fisher Chemical) containing the sample on a Lacey carbon grid. Scanning Electron Microscopy (SEM) was performed on a Zeiss Gemini SEM 300 electron microscope with acceleration voltage of 3 kV and with Everhart-Thornley secondary electron detector to study the morphology of the clay particles. For EDX analysis, the microscope was equipped with an Oxford detector X-max^N and EDX measurements were performed by means of AZtec software. To acquire X-rays signal from all elements present in the sample, an e-beam acceleration voltage of 6 kV was applied.

Magic angle spinning nuclear magnetic resonance (MAS-NMR) was used to study the coordination and chemical environment of Al, Si and Sn. ^{27}Al and ^{29}Si spectra were collected on a 400 MHz Bruker Avance III HD spectrometer with a spinning rate of 35 and 15 kHz, respectively. ^{119}Sn spectra were recorded at room temperature on a 500 MHz Bruker instrument equipped with a 11.7 T magnet (proton frequency) with a spinning rate of 20 kHz. All spectra were recorded at 298 K with a single-pulse and the typical acquisition was 1024 scans. ^{1}H MAS-NMR was also performed but did not provide reproducible results and is therefore not included.

The concentration of acid sites was calculated from NH_3 temperature programmed desorption (NH_3-TPD) experiments using a Micromeritics Autochem 2920 II instrument. Typically, the sample (ca. 100 mg) was loaded in a U-shaped quartz cell and dried with a He flow (50 mL min^{-1}) at 200 °C (2 °C min^{-1}; hold time of 120 min). Saturation of the sample with NH_3 was done using a 1:99 NH_3:He (volumetric ratio) flow during 1 h at 50 °C. Physisorbed NH_3 was then removed with He (50 mL min^{-1}). The temperature was then increased to 600 °C (10 °C min^{-1}) and NH_3 desorption was monitored using a calibrated MKS Cirrus II mass spectrometer (mass 16).

Diffuse reflectance infrared Fourier transform spectroscopy (DRIFTS) was performed on a high temperature Harrick DRIFT cell mounted on a Perkin Elmer Frontier spectrometer equipped with a mercury cadmium telluride detector. Ex-situ spectra were recorded with 32 scans at a resolution of 4 cm^{-1} after being dried 2 h at 200 °C under a He flow of 20 mL·min^{-1}. Pyridine adsorption experiments were performed using the following procedure: first, the sample was dried and consequently saturated with pyridine vapor at 50 °C for 30 min under a He flow of 20 mL min^{-1} bubbling through pyridine at room temperature. Physisorbed pyridine was then removed by flowing pure He (20 mL min^{-1}) for 30 min. Finally, the temperature was raised to 150 and 300 °C with a ramp rate of 5 °C^{-1}.

Catalytic tests

Synthesis of OME were performed in two setups described in Figure 8. The first is a 450 mL stirred batch reactor manufactured in
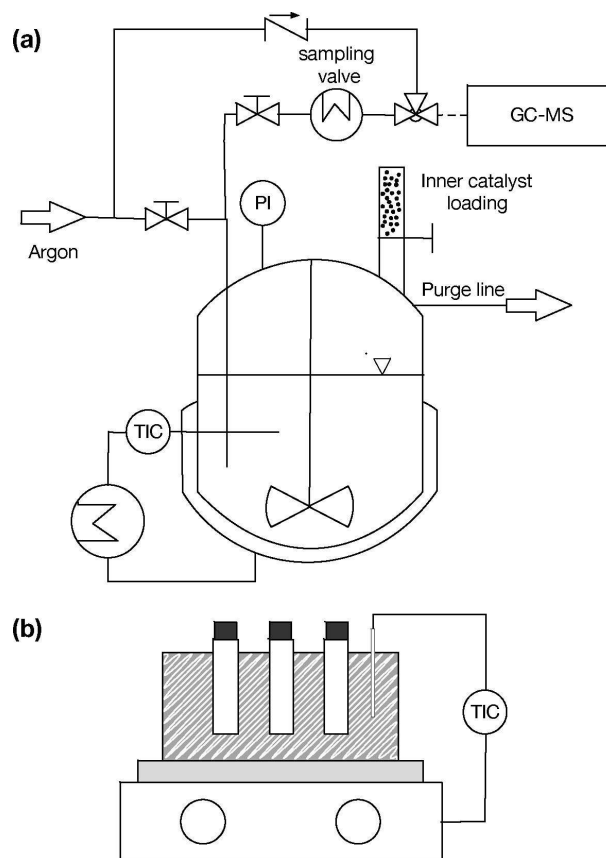

Figure 8. Schematic of (a) the 450 mL stirred batch reactor and (b) glass reactors in the aluminum block on a stirring plate. PI: pressure indicator. TIC: temperature indicator and control. PIC: pressure indicator and control.

316 stainless steel under a pressure of 5 bar of Ar. Typically, 30.83 g of TRI and 85.93 g of OME_1 were loaded followed by 3 purges of Ar prior to mixing and heating the mixture to the reaction temperature (Figure 8a). The temperature and pressure were measured respectively with a J-type thermocouple and a membrane pressure gauge. The reactor was thermostated with an electrically heated jacket. A stirring speed of 450 rpm was used. Samples (0.3 mL) were taken from the bottom of the reactor using a sample valve composed of a dip tube and a heat exchanger to cool the samples at 30 °C. Catalyst injection was performed using a pressurized solid charging system and was considered as the start of the reaction.

The second setup was composed of glass reactors (Grace, 10 mL) with PTFE screw caps and a silicon sealing disk (Figure 8b) heated by an aluminum block with holes using a magnetic stirring (450 rpm). After loading with the reactants and catalyst, the reactors were inserted into the aluminum block, which was considered as the start of the reaction. A sample was taken after quenching the reactors in an ice bath. Unless mentioned otherwise, all experiments were conducted at 70 °C with a OME_1/TRI molar ratio of 3.3 and 0.5 wt.% of catalyst. A catalyst loading of 1.0 wt.% was used for the reusability test with a reaction time of 60 min.

An Agilent 7890B/5977A series gas chromatography mass spectrometer (GC-MS) was used for the analysis of the liquid samples. It was equipped with an HP-5 capillary column (length 30 m, outer diameter 0.32 mm, film 1.05 µm) and an automated liquid sampler. A dean switch was used to send the eluent to a Flame Ionization Detector (FID) or to the mass spectrometer. OME_{1-6}, methanol and methyl formate were quantified using a calibration curve. OME_{7-8} calibration curves were constructed based on the effective carbon number method and an extrapolation of the detector response from OME_{1-6}.[62] Conversion of trioxane (X_{TRI}), selectivity to OME_{3-5} ($S(OME_{3-5})$) and growth probability (α) were used to quantify the performance of the catalysts for the synthesis of OME and were defined as [Eq. (2)-(4)]:

$$X_{TRI} = \frac{[TRI]_0 - [TRI]}{[TRI]_0} \qquad (2)$$

$$S(OME_{3-5}) = \frac{\sum_{i=3}^{5}[OME]_i}{\sum_{i=2}^{8}[OME]_i} \qquad (3)$$

$$\log\alpha = \frac{\log[OME]_{n+1} - \log[OME]_n}{n} \qquad (4)$$

Acknowledgements

Conflict of Interest

The authors declare no conflict of interest.

Keywords: Polyoxymethylene dimethyl ethers · oxygenated fuel · tin · clays · hierarchical material

[1] B. Lumpp, D. Rothen, C. Pastötter, R. Lämmermann, E. Jacob, *MTZ* **2011**, *72*, 34–39.
[2] J. Burger, M. Siegert, E. Ströfer, H. Hasse, *Fuel* **2010**, *89*, 3315–3319.
[3] E. Jacob, W. Maus, *MTZ Worldw.* **2017**, *3*.
[4] K. Hackbarth, P. Haltenort, U. Arnold, *Chem. Ing. Tech.* **2018**, *90*, 1520–1528.
[5] J. Burger, E. Ströfer, H. Hasse, *Ind. Eng. Chem. Res.* **2012**, *51*, 12751–12761.
[6] Q. Zhao, H. Wang, Z. Qin, Z. Wu, J. Wu, W. Fan, J. Wang, *J. Fuel Chem. Technol.* **2011**, *39*, 918–923.
[7] L. Wang, W.-T. Wu, T. Chen, Q. Chen, M.-Y. He, *Chem. Eng. Commun.* **2014**, *201*, 709–717.
[8] C. J. Baranowski, A. M. Bahmanpour, O. Kröcher, *Appl. Catal. B* **2017**, 407–420.
[9] H. Li, H. Song, L. Chen, C. Xia, *Appl. Catal. B* **2015**, *165*, 466–476.
[10] Y. Zheng, Q. Tang, T. Wang, Y. Liao, J. Wang, *Chem. Eng. Technol.* **2013**, *36*, 1951–1956.
[11] Z. Xue, H. Shang, Z. Zhang, C. Xiong, C. Lu, G. An, *Energy Fuels* **2016**, *31*, 279–286.
[12] J. Qi, Y. Hu, S. Jiang, W. Ma, Z. Yang, Y. Wang, *Fuel* **2019**, *245*, 521–527.
[13] D. Oestreich, L. Lautenschütz, U. Arnold, J. Sauer, *Chem. Eng. Sci.* **2017**, *163*, 92–104.
[14] L. Lautenschütz, D. Oestreich, P. Haltenort, U. Arnold, E. Dinjus, J. Sauer, *Fuel Process. Technol.* **2017**, *165*, 27–33.
[15] J. Guilera, E. Ramírez, C. Fité, M. Ibora, J. Tejero, *Appl. Catal. A* **2013**, *467*, 301–309.
[16] C. J. Baranowski, A. M. Bahmanpour, F. Héroguel, J. S. Luterbacher, O. Kröcher, *Catal. Sci. Technol.* **2019**, *9*, 366–376.
[17] H. H. Murray, *Appl. Clay Sci.* **1991**, *5*, 379–395.
[18] H. H. Murray, *Appl. Clay Sci.* **2000**, *17*, 207–221.
[19] Z. Ding, J. T. Kloprogge, R. L. Frost, *J. Porous Mater.* **2001**, *8*, 273–293.
[20] A. M. Bahmanpour, F. Héroguel, C. J. Baranowski, J. S. Luterbacher, O. Kröcher, *Appl. Catal. A* **2018**, *560*, 165–170.
[21] F. Uddin, *Metall. Mater. Trans. A* **2008**, *39*, 2804–2814.
[22] J. T. Kloprogge, *J. Porous Mater.* **1998**, *5*, 5–41.
[23] Y. Masui, J. Wang, K. Teramura, T. Kogure, T. Tanaka, M. Onaka, *Microporous Mesoporous Mater.* **2014**, *198*, 129–138.
[24] S. Shinde, C. Rode, *Catal. Commun.* **2017**, *88*, 77–80.
[25] J. Wang, Y. Masui, K. Watanabe, M. Onaka, *Adv. Synth. Catal.* **2009**, *351*, 553–557.
[26] J. Wang, Y. Masui, M. Onaka, *Tetrahedron Lett.* **2010**, *51*, 3300–3303.
[27] J. Wang, Y. Masui, M. Onaka, *Eur. J. Org. Chem.* **2010**, 1763–1771.
[28] J. Wang, Y. Masui, M. Onaka, *ACS Catal.* **2011**, *1*, 446–454.
[29] J. Wang, J. Ren, X. Liu, J. Xi, Q. Xia, Y. Zu, G. Lu, Y. Wang, *Green Chem.* **2012**, *14*, 2506–2512.
[30] J. Wang, Y. Masui, M. Onaka, *Appl. Catal. B* **2011**, *107*, 135–139.
[31] H. Li, J. Ren, L. Zhong, R. Sun, L. Liang, *Bioresour. Technol.* **2015**, *176*, 242–248.
[32] T. Hara, M. Hatakeyama, A. Kim, N. Ichikuni, S. Shimazu, *Green Chem.* **2012**, *14*, 771–777.
[33] A. Neaman, M. Pelletier, F. Villieras, *Appl. Clay Sci.* **2003**, *22*, 153–168.
[34] K. Bahranowski, A. Gaweł, A. Klimek, A. Michalik-Zym, B. D. Napruszewska, M. Nattich-Rak, M. Rogowska, E. M. Serwicka, *Appl. Clay Sci.* **2017**, *140*, 75–80.
[35] L. Le Forestier, F. Muller, F. Villieras, M. Pelletier, *Appl. Clay Sci.* **2010**, *48*, 18–25.
[36] V. K. Soni, R. K. Sharma, *ChemCatChem* **2016**, *8*, 1763–1768.
[37] V. K. Soni, P. R. Sharma, G. Choudhary, S. Pandey, R. K. Sharma, *ACS Sustainable Chem. Eng.* **2017**, *5*, 5351–5359.
[38] P. J. Wallis, W. P. Gates, A. F. Patti, J. L. Scott, E. Teoh, *Green Chem.* **2007**, *9*, 980.
[39] J. Madejová, *Vib. Spectrosc.* **2003**, *31*, 1–10.
[40] B. Tyagi, C. D. Chudasama, R. V. Jasra, *Spectrochim. Acta Part A* **2006**, *64*, 273–278.
[41] L. Yan, C. B. Roth, P. F. Low, *J. Colloid Interface Sci.* **1996**, *184*, 663–670.
[42] S. Cadars, R. Guégan, M. N. Garaga, X. Bourrat, L. Le Forestier, F. Fayon, T. V. Huynh, T. Allier, Z. Nour, D. Massiot, *Chem. Mater.* **2012**, *24*, 4376–4389.
[43] N. N. Binitha, S. Sugunan, *Microporous Mesoporous Mater.* **2006**, *93*, 82–89.
[44] A. Phukan, S. J. Borah, P. Bordoloi, K. Sharma, B. J. Borah, P. P. Sarmah, D. K. Dutta, *Adv. Powder Technol.* **2017**, *28*, 1585–1592.
[45] C. Eypert-Blaison, L. J. Michot, B. Humbert, M. Pelletier, F. Villiéras, J. B. D'Espinose de la Caillerie, *J. Phys. Chem. B* **2002**, *106*, 730–742.
[46] D. Amalric-Popescu, F. Bozon-Verduraz, *Catal. Today* **2001**, *70*, 139–154.
[47] R. Alvero, M. D. Alba, M. A. Castro, J. M. Trillo, *J. Phys. Chem.* **1994**, *98*, 7848–7853.
[48] W. Jones, *Catal. Today* **1988**, *2*, 357–367.
[49] N. J. Clayden, C. M. Dobson, A. Fern, *J. Chem. Soc. Dalton Trans.* **1989**, 843–847.
[50] S. Indris, M. Scheuermann, S. M. Becker, V. Šepelák, R. Kruk, J. Suffner, F. Gyger, C. Feldmann, A. S. Ulrich, H. Hahn, *J. Phys. Chem. C* **2011**, *115*, 6433–6437.
[51] J. Chen, X. P. Wu, L. Shen, Y. Li, D. Wu, W. Ding, X. Q. Gong, M. Lin, L. Peng, *Chem. Phys. Lett.* **2016**, *643*, 126–130.
[52] P. Ferrini, J. Dijkmans, R. De Clercq, S. Van de Vyver, M. Dusselier, P. A. Jacobs, B. F. Sels, *Coord. Chem. Rev.* **2017**, *343*, 220–255.
[53] C. Fan, Y. Peng, Q. Zhu, L. Lin, R. Wang, A. Xu, *J. Phys. Chem. C* **2013**, *117*, 24157–24166.
[54] Y. Yang, Y. Wang, S. Yin, *Appl. Surf. Sci.* **2017**, *420*, 399–406.

[55] H. Wang, K. Dou, W. Y. Teoh, Y. Zhan, T. F. Hung, F. Zhang, J. Xu, R. Zhang, A. L. Rogach, *Adv. Funct. Mater.* **2013**, *23*, 4847–4853.

[56] T. Barzetti, E. Selli, D. Moscotti, L. Forni, *J. Chem. Soc. Faraday Trans.* **1996**, *92*, 1401.

[57] J.-F. Lambert, G. Poncelet, *Top. Catal.* **1997**, *4*, 43–56.

[58] S. Ghosh, L. Manna, *Chem. Rev.* **2018**, *118*, 7804–7864.

[59] F. Liu, T. Wang, Y. Zheng, J. Wang, *J. Catal.* **2017**, *355*, 17–25.

[60] K. Beloufa, N. Sahli, M. Belbachir, *J. Appl. Polym. Sci.* **2009**, *115*, 2820–2827.

[61] S. Das, V. Jayaraman, *Prog. Mater. Sci.* **2014**, *66*, 112–255.

[62] J. T. Scanlon, D. E. Willis, *J. Chromatogr. Sci.* **1985**, *23*, 333–340.